

Supporting Information:

Changing Face: A Key Residue for the Addition of Water by Sclareol Synthase

Meirong Jia,[†] Terrence E. O'Brien,[‡] Yue Zhang,[‡] Justin B. Siegel,^{‡,§,‡} Dean J. Tantillo,[‡] and
Reuben J. Peters^{†,*}

[†]Roy J. Carver Department of Biochemistry, Biophysics and Molecular Biology, Iowa State University, Ames, IA, 50011, USA

[‡]Department of Chemistry, University of California, Davis, CA, 95616, USA

[§]Department of Biochemistry and Molecular Medicine, University of California Davis, Davis, CA, 95616, USA

[‡]Genome Center, University of California Davis, Davis, CA, 95616, USA

*Corresponding author: email: rjpeters@iastate.edu

Content

S1-S7: Materials and methods

S8: Figure S1. Mutational effect of S433 and T436 residues on SsSS product outcome.

S8: Figure S2. Identification of the enzymatic product **3**.

S8: Figure S3. Comparison of product formation by SsSS variants with **1** *in vivo*.

S9: Figure S4. Mutational effect of N431 from non-chiral column analysis.

S9: Figure S5. Mutational effect of N431 from chiral column analysis.

S9: Figure S6. The two oxygens in the diphosphate complex are pointed into the pocket.

S10: Figure S7. Heat map for predicting the catalytically relevant oxygen.

S10: Figure S8. The low energy structures identified by the docking simulations.

S11: Figure S9. Mutational effect of N431 from non-chiral column analysis.

S11: Figure S10. Mutational effect of N431 from chiral column analysis.

S12: Figure S11. Comparison of product formation by SsSS variants with **4** *in vivo*.

S12: Table S1. Primers for mutagenesis

Materials and Methods

General. Unless otherwise noted, chemicals were purchased from Fisher Scientific and molecular biology reagents from Invitrogen.

Sequence analysis. Alignment was carried out with CLC Main Workbench (version 7). The various diterpene synthases shown in Figure 1A are CfMOS, manoyl oxide synthase from

Coleus forskohlii (GenBank accession: KF444508);¹ IrMS, miltiradiene synthase from *Isodon rubescens* (KX831652);² CfMS, miltiradiene synthase from *C. forskohlii* (KF444509);¹ RoMS1, miltiradiene synthase 1 from *Rosemarium officinalis* (KF805858);³ SmMS, miltiradiene synthase from *Salvia miltiorrhiza* (ABV08817);⁴ RoMS2, miltiradiene synthase 2 from *Rosemarium officinalis* (KF805859);³ SfMS, miltiradiene synthase from *Salvia fruticosa* (KP091841);⁵ MvELS, 9,13-epoxy-labd-14-ene synthase from *Marrubium vulgare* (KJ584454);⁶ SsSS, sclareol synthase from *Salvia sclarea* (JN133922).⁷

Mutant construction. The SsSS utilized here was the previously described pseudomature construct suitable for recombinant expression in *E. coli*.⁸ Site-directed mutants were constructed by whole-plasmid PCR amplification of the relevant pENTR/SD/D-TOPO constructs using the primers described in Table S1, and AccuPrime™ Pfx DNA Polymerase. All mutants were verified by complete gene sequencing and then transferred via directional recombination to the T7-based expression vector pDEST14.

Metabolic engineering. To determine product outcome, SsSS (wild-type or mutant) was transformed into *E. coli* strain C41 OverExpress (Lucigen), along with plasmids that enabled production of the substrates (i.e., **1** or **4**) studied here, as previously described.⁸ The resulting recombinant strains were cultured in 50 mL TB medium (pH = 7.0), with appropriate antibiotics, in 250 mL Erlenmeyer flasks. These cultures were first grown by shaking at 37 °C to mid-log phase (OD₆₀₀ ~0.7), then the temperature dropped to 16 °C for 0.5 h before induction with 1 mM isopropylthiogalactoside (IPTG) and supplementation with 40 mM sodium pyruvate and 1 mM MgCl₂. The induced cultures were further grown for an additional three days before extraction with an equal volume (50 mL) of hexanes, with the organic phase then separated, and concentrated under N₂ when necessary. For product yield comparison, three replicates for each SsSS variant were grown in parallel and during extraction, 50 uL hexane with 15 uM cembrene as the internal standard added. The 1 uL of top organic layer has been directly injected into GC-MS for analysis, with the area under the relevant product peak used for quantification.

Kinetic analysis. To enable purification, the targeted enzymes were individually cloned into pDEST17, expressed in *E. coli* strain C41 OverExpress, without any other plasmids, and grown as above. The resulting N-terminally 6xHis-tagged enzymes were purified by passing cell-free lysates over Ni-NTA His-bind resin (Novagen), washing with buffer A (50 mM MOPSO, pH 6.8, 300 mM NaCl, 10% glycerol and 10 mM imidazole), and eluting with buffer B (imidazole concentration increased to 250 mM). Eluted proteins were dialyzed in 12-14 kDa MW Cutoff tubing against storage buffer (50 mM MOPSO (pH 6.8), 1 mM DTT, 10% glycerol) overnight.

In vitro assays were carried out by using freshly purified NgCLS enzyme to convert GGPP (Isoprenoids) to 8 α -hydroxy-copalyl diphosphate (**1**). Briefly, 1.5 μ M NgCLS was added into assay buffer 1 (50 mM HEPES, pH 7.2, 0.1 mM MgCl₂, 100 mM KCl, 10% glycerol, and 5 mM DTT) with 200 μ M GGPP and let react overnight at 30 °C. Conversion to **1** was verified by enzymatic dephosphorylation by calf intestinal alkaline phosphatase (Promega) and GC-MS analysis of a small aliquot. The remaining solution was utilized as a substrate stock solution. SsSS assays were performed in 0.2-ml reaction volumes in assay buffer 2 (mM HEPES, pH 7.2, 7.5 mM MgCl₂, 100 mM KCl, 10% glycerol, and 5 mM DTT), using 10 nM enzyme, and variable concentrations of freshly made **1** (1 to 100 μ M). All the reaction ingredients except SsSS were mixed in 1.5-ml screw-top glass vials and pre-incubated in a 30 °C water bath for 15 min, then the reaction initiated by the addition of enzyme. The reaction was run at 30 °C for 10 min and terminated by the addition of KOH to 0.2 M and EDTA to 15 mM, with vigorous mixing (vortexing) for 5 s. Then an equal volume of organic solvent (ethyl acetate:hexane = 3:1) with 5 μ M cembrene as the internal standard was subsequently added to extract the enzymatic product by vortexing for 15 s. The organic layer was carefully separated, 100 μ L of which was dried under a steady stream of N₂ and redissolved in 50 μ L hexane for GC-MS analysis (see below). All assays were performed in triplicate with GC-MS data collected in the total ion current mode. Authentic standards were commercially available (sclareol, **2**) or previously isolated (isoabienol, **3**), and were prepared in serial dilutions of known concentration (ranging from 0.4 μ M to 50 μ M) for construction of calibration curves based on peak area integration. The resulting data as analyzed using Kaleidagraph (Synergy Software, Reading, PA, USA).

Product analyses. Gas chromatography with mass spectral detection (GC-MS) was carried on a Varian 3900 GC with a Saturn 2100T ion trap mass spectrometer in electron ionization (70 eV) mode. For non-chiral analyses, an Agilent HP-5MS column (Agilent, 19091S-433) was used with 1.2 mL/min helium flow rate. Samples (1 μ L) as prepared above were injected in splitless mode by an 8400 autosampler with the injection port set at 250 °C. The following temperature program was used: the oven temperature initially started at 50 °C, which was maintained for 3 min, and then increased at a rate of 15 °C/min to 300 °C, where it was held for another 3 min. Mass spectrum was recorded by mass-to-charge ratio (m/z) values in a range from 90 to 650, starting from 13 min after sample injection until the end of the run. Enzymatic products were identified by comparison of retention time and mass spectra to those of authentic standards. GC-MS area under curve (AUC) was calculated from automated analyses for product quantitation. For chiral analyses, an Agilent CYCLOSIL-B column (Agilent, USN 198416H) was utilized. Specifically, for analyzing sclareols (**2a** and **2b**), the following program was employed. The helium flow rate was set as 1.0 mL/min and the injection port was set at 200 °C and the oven temperature initially started at 50 °C, which was maintained for 3 min, and then increased at a rate of 2 °C/min to 225 °C, where it was held for another 3 min. Mass spectrum was recorded starting from 60 min after sample injection until the end of the run. For analyzing manools (**5a** and **5b**), the program was modified as follows: the helium flow rate was set as 1.1 mL/min, and the oven temperature was ramping up by 1 °C/min to 215 where it was held for another 3 min. And the mass record started from 90 min after injection until the end of the run. All other parameters were the same the non-chiral analysis described above.

Docking simulation study. A three-dimensional model of SsSS was generated using the RosettaCM protocol.⁹ Templates for generating the models were seven crystal structures that have been identified to be in a closed state, namely class I terpene synthases which have a diphosphate (PP_i) and three magnesium ions (Mg²⁺) bound in the active site. The PDB codes for the seven templates are 2ONG, 1JFG, 1N21, 2OA6, 3KB9, 4OKZ and 5IKA. A multiple sequence alignment was generated from the sequences of these templates and the query

sequence to correlate sequence position to structure using Promals3D.¹⁰ To fill in unaligned regions during molecular modeling, structural fragment sets were generated using standard methods.¹¹ During multi-template fragment based modeling through RosettaCM, evolutionary constraints were used to enhance sampling.¹² The Mg and PP_i were treated as a single ligand complex and it was incorporated as a centroid as the homology models were constructed. In addition, the residues of the DDXXD and NSE motifs, which are required for ionization of the PP_i,¹³ were constrained to the complex to obtain the catalytic relevant pose. Using this protocol, 5000 decoys of the SsSS were generated and the five lowest energy models were selected as templates for ligand docking.

A conformational search for 13*R*-sclareol was performed using Spartan'16 (Wavefunction), which identified 357 conformers that were used without further optimization. A diphosphate/magnesium complex was extracted from that found in one of the utilized class I terpene synthase crystal structures (PDB ID: 2ONG), and this was docked (unchanged) along with the previously generated conformer library into the five low energy homology models using the Rosetta Modeling Suite,¹⁴⁻¹⁶ using the taleris2013 score function.¹⁷⁻¹⁹ As conducted previously,²⁰ the docking was performed using chemically meaningful constraints. In particular, using a set of constraints between the unrelaxed magnesium/diphosphate complex oxygens and the carbon that was previously attached to the diphosphate. There are two oxygens pointed into the active site for the selected complex, which of these oxygens was previously bound to the carbon of the substrate was unknown, so 500 docking simulations, with a distance constraint of $3.0 \text{ \AA} \pm 0.5 \text{ \AA}$, was performed for both options. The results were pooled and filtered by: 1) their ability to meet the constraints – structures that did not satisfy the constraints were not considered, 2) total protein energy – only structures that were within one standard deviation or lower than the mean were considered, 3) interface energy – the top 10% in interface energy were selected from the structures that were in the low total protein energy population. After filtering, the remaining structures were separated based on which oxygen they had been constrained to during the docking – i.e. after determining what structures best fit these criteria, to which oxygen had they been constrained. These final filtered structures were then grouped by binding orientation to identify where the low energy population resided shown as a heat map in **Figure S7**. For the majority of the

homology models, oxygen A is predicted to be the likely point of diphosphate attachment and only poses from this orientation are predicted to be catalytically relevant. As with our other modelling of terpene synthases, the interface energy (docking score) does not appear to be predictive of what pose is more relevant to catalysis. The low energy docking results into each homology model are shown in **Figure S8A**. Unfortunately, the pose predicted by each different homology does not converge to a single answer. This prevents us from making confident prediction about the molecular details of how the different residues may affect the product profile and further highlight the caution that should be applied when considering the use of homology models for such docking analyses. Three of the models do converge to similar structures as shown in **Figure S8B**. These models potentially predict why the S433C and T436C mutations did not affect the product profile – as these are distal from the added hydroxyl group and the substituted residues have roughly the same shape. The models also suggest that the N431Q mutant may not directly affecting water incorporation, but rather affect preorganization of the substrate. For the sake of clarity only one model is shown in the main text – i.e., homology model four, which is shown again here as **Figure S8C** for comparative purposes.

References:

1. Pateraki, I.; Andersen-Ranberg, J.; Hamberger, B.; Heskes, A. M.; Martens, H. J.; Zerbe, P.; Bach, S. S.; Moller, B. L.; Bohlmann, J.; Hamberger, B. Manoyl Oxide (13R), the Biosynthetic Precursor of Forskolol, Is Synthesized in Specialized Root Cork Cells in *Coleus forskohlii*. *Plant Physiol.* **2014**, *164*, 1222-36.
2. Pelot, K. A.; Hagelthorn, D. M.; Addison, J. B.; Zerbe, P. Biosynthesis of the oxygenated diterpene nezukol in the medicinal plant *Isodon rubescens* is catalyzed by a pair of diterpene synthases. *PLoS One* **2017**, *12*, e0176507.
3. Brückner, K.; Bozic, D.; Manzano, D.; Papaefthimiou, D.; Pateraki, I.; Scheler, U.; Ferrer, A.; de Vos, R. C.; Kanellis, A. K.; Tissier, A. Characterization of two genes for the biosynthesis of abietane-type diterpenes in rosemary (*Rosmarinus officinalis*) glandular trichomes. *Phytochemistry* **2014**, *101*, 52-64.
4. Gao, W.; Hillwig, M. L.; Huang, L.; Cui, G.; Wang, X.; Kong, J.; Yang, B.; Peters, R. J. A functional genomics approach to tanshinone biosynthesis provides stereochemical insights. *Org. Lett.* **2009**, *11*, 5170-5173.
5. Bozic, D.; Papaefthimiou, D.; Bruckner, K.; de Vos, R. C.; Tsoleridis, C. A.; Katsarou, D.; Papanikolaou, A.; Pateraki, I.; Chatzopoulou, F. M.; Dimitriadou, E.; Kostas, S.; Manzano, D.; Scheler, U.; Ferrer, A.; Tissier, A.; Makris, A. M.; Kampranis, S. C.; Kanellis, A. K. Towards Elucidating Carnosic Acid Biosynthesis in Lamiaceae: Functional Characterization of the Three First Steps of the Pathway in *Salvia fruticosa* and *Rosmarinus officinalis*. *PLoS One* **2015**, *10*, e0124106.
6. Zerbe, P.; Chiang, A.; Dullat, H.; O'Neil-Johnson, M.; Starks, C.; Hamberger, B.; Bohlmann, J. Diterpene

synthases of the biosynthetic system of medicinally active diterpenoids in *Marrubium vulgare*. *Plant J.* **2014**, *79*, 914-27.

7. Schalk, M.; Pastore, L.; Mirata, M. A.; Khim, S.; Schouwey, M.; Deguerry, F.; Pineda, V.; Rocci, L.; Daviet, L. Towards a Biosynthetic Route to Sclareol and Amber Odorants. *J. Am. Chem. Soc.* **2012**, *134*, 18900-18903.

8. Jia, M.; Potter, K. C.; Peters, R. J. Extreme promiscuity of a bacterial and a plant diterpene synthase enables combinatorial biosynthesis. *Metab. Eng.* **2016**, *37*, 24-34.

9. Song, Y.; DiMaio, F.; Wang, R. Y.; Kim, D.; Miles, C.; Brunette, T.; Thompson, J.; Baker, D. High-resolution comparative modeling with RosettaCM. *Structure* **2013**, *21*, 1735-42.

10. Pei, J.; Grishin, N. V. PROMALS3D: multiple protein sequence alignment enhanced with evolutionary and three-dimensional structural information. *Methods Mol. Biol.* **2014**, *1079*, 263-71.

11. Gront, D.; Kulp, D. W.; Vernon, R. M.; Strauss, C. E.; Baker, D. Generalized fragment picking in Rosetta: design, protocols and applications. *PLoS One* **2011**, *6*, e23294.

12. Thompson, J.; Baker, D. Incorporation of evolutionary information into Rosetta comparative modeling. *Proteins* **2011**, *79*, 2380-8.

13. Christianson, D. W. Structural and Chemical Biology of Terpenoid Cyclases. *Chem. Rev.* **2017**, *117*, 11570-11648.

14. Meiler, J.; Baker, D. ROSETTALIGAND: protein-small molecule docking with full side-chain flexibility. *Proteins* **2006**, *65*, 538-48.

15. Fleishman, S. J.; Leaver-Fay, A.; Corn, J. E.; Strauch, E. M.; Khare, S. D.; Koga, N.; Ashworth, J.; Murphy, P.; Richter, F.; Lemmon, G.; Meiler, J.; Baker, D. RosettaScripts: a scripting language interface to the Rosetta macromolecular modeling suite. *PLoS One* **2011**, *6*, e20161.

16. Combs, S. A.; Deluca, S. L.; Deluca, S. H.; Lemmon, G. H.; Nannemann, D. P.; Nguyen, E. D.; Willis, J. R.; Sheehan, J. H.; Meiler, J. Small-molecule ligand docking into comparative models with Rosetta. *Nat. Protoc.* **2013**, *8*, 1277-98.

17. Leaver-Fay, A.; O'Meara, M. J.; Tyka, M.; Jacak, R.; Song, Y.; Kellogg, E. H.; Thompson, J.; Davis, I. W.; Pache, R. A.; Lyskov, S.; Gray, J. J.; Kortemme, T.; Richardson, J. S.; Havranek, J. J.; Snoeyink, J.; Baker, D.; Kuhlman, B. Scientific benchmarks for guiding macromolecular energy function improvement. *Methods Enzymol.* **2013**, *523*, 109-43.

18. Song, Y.; Tyka, M.; Leaver-Fay, A.; Thompson, J.; Baker, D. Structure-guided forcefield optimization. *Proteins* **2011**, *79*, 1898-909.

19. Shapovalov, M. V.; Dunbrack, R. L., Jr. A smoothed backbone-dependent rotamer library for proteins derived from adaptive kernel density estimates and regressions. *Structure* **2011**, *19*, 844-58.

20. O'Brien, T. E.; Bertolani, S. J.; Tantillo, D. J.; Siegel, J. B. Mechanistically informed predictions of binding modes for carbocation intermediates of a sesquiterpene synthase reaction. *Chem. Sci.* **2016**, *7*, 4009-4015.

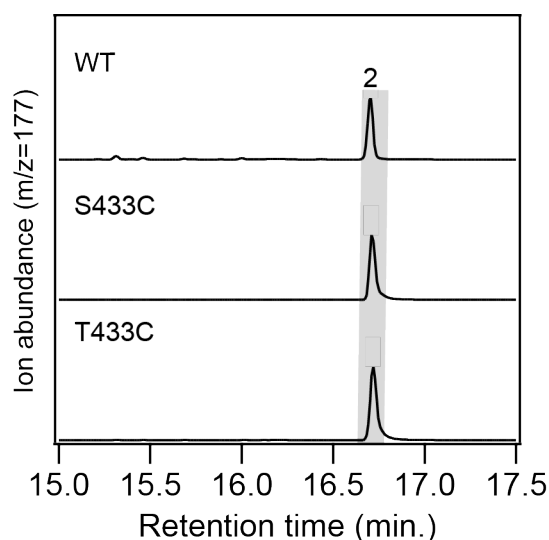


Figure S1. Mutational effect on SsSS product outcome. Chromatograms from GC–MS analysis of the products from **1** with wild-type (WT) or indicated mutants of SsSS (**2**, sclareol).

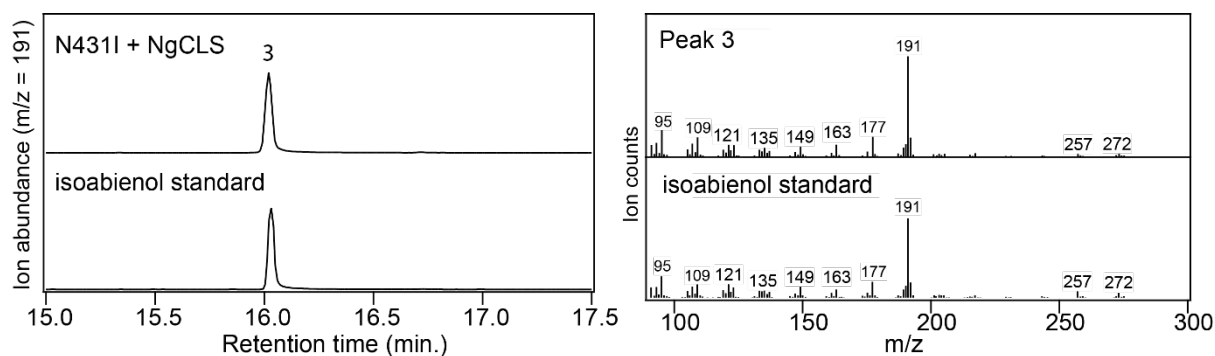


Figure S2. Identification of the enzymatic product **3**. GC-MS chromatograms comparing both retention time and mass spectrum of the enzymatic product to an authentic standard of isoabienol.

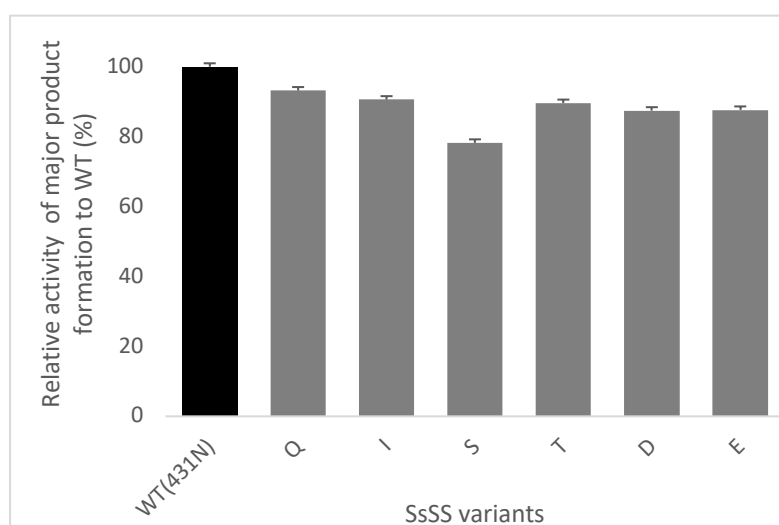


Figure S3. Biosynthetic yield of SsSS variants relative to wild-type (WT) with **1** from metabolically engineered *E. coli*. The relevant product was quantified using cembrene as an internal standard ($n = 3$, values represent the average of three cultures with the standard deviation shown).

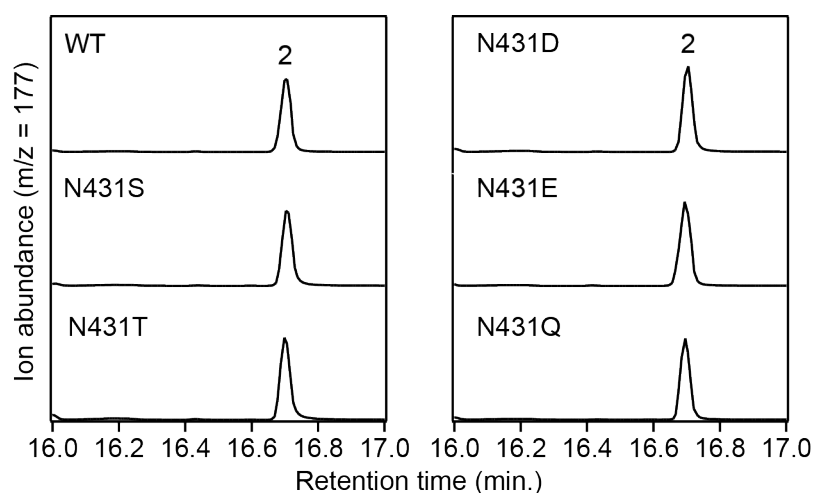


Figure S4. Polar substitutions of N431 do not block the addition of water to **1** by SsSS. Chromatograms from GC–MS analysis.

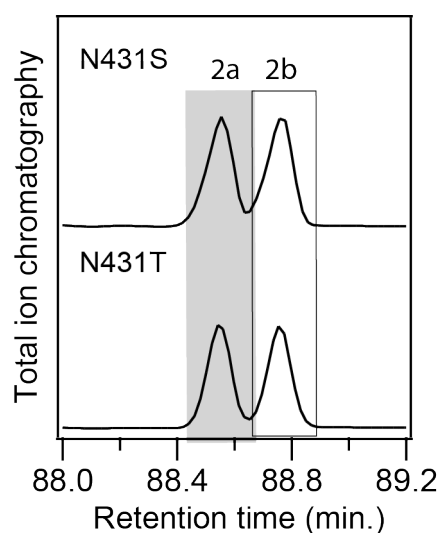


Figure S5. Substitution of hydroxyl containing residues for N431 does not alter SsSS product stereochemistry with **1**. Chromatograms from chiral GC–MS analysis of **2** produced by wild-type (WT) or indicated mutants of SsSS from **1** (lettering correspond to the 13-epimers as defined in the text).

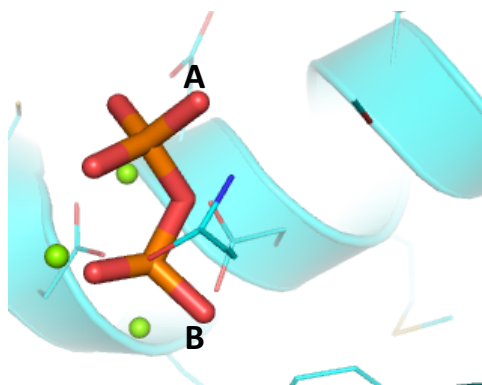


Figure S6. The two oxygens in the diphosphate complex are pointed into the pocket are labeled as **A** and **B**.

	Oxygen A	Oxygen B
Homology Model 1	65.4% <i>17</i> <u>-7.47</u>	34.6% <i>9</i> <u>-7.37</u>
Homology Model 2	86.8% <i>33</i> <u>-7.09</u>	13.2% <i>5</i> <u>-6.64</u>
Homology Model 3	36.4% <i>4</i> <u>-7.88</u>	63.6% <i>7</i> <u>-7.92</u>
Homology Model 4	90.9% <i>30</i> <u>-7.89</u>	9.1% <i>3</i> <u>-8.09</u>
Homology Model 5	82.4% <i>14</i> <u>-7.15</u>	17.6% <i>3</i> <u>-7.13</u>

Figure S7. Heat map for predicting the catalytically relevant oxygen for the homology models. The darker the color in each square is a qualitative representation of the prediction for which oxygen is likely to have bound to the oxygen. There are three numbers listed for the docking results for each oxygen. The numbers in each box are as follows: in bold are the percentage of structures for the constraint to that oxygen, in italics are the number of structures and underlined is the average interface energy (docking score). Only homology model four gave rise to a prediction about which oxygen but that model is consistent with the prediction made by the majority of the other homology models.

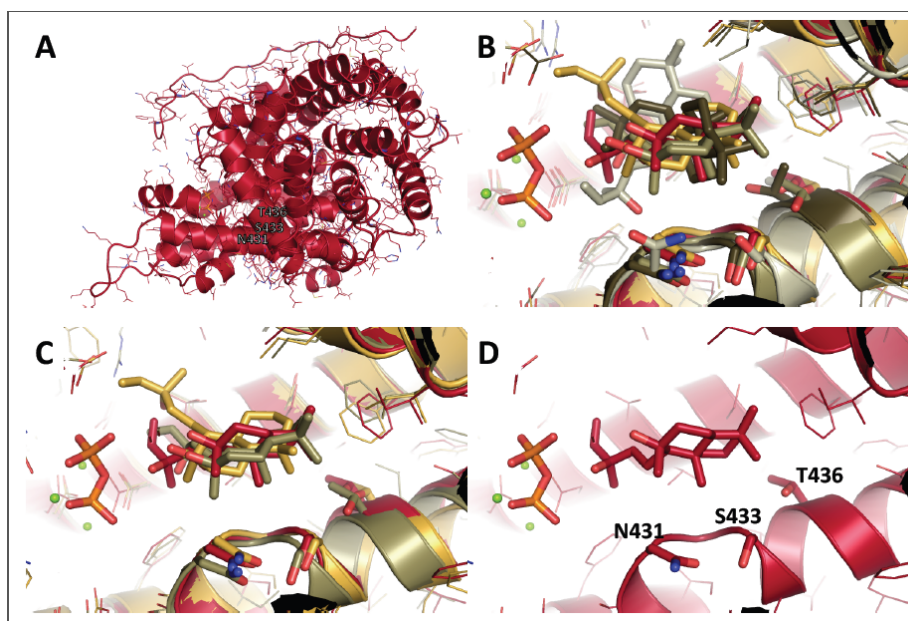


Figure S8. Homology modeling and docking. Homology model one is represented in olive, homology model two is drawn in yellow, homology model three is in tan, homology model is drawn in red and homology model 5 is in white. The side chains are represented as lines except for the points of mutations which are shown as sticks. (A) The entire structure of homology model 4. The three mutated residues are indicated to define the active site. (B) The overlay of a low energy docking result for each homology model in the same orientation as in (A). The models do not converge to a single answer. (C) Overlay of homology models two, three and four. In these models, 13R-sclareol converges to a single region in space. (D) The low energy structure from homology model 4, which had the strongest prediction for which oxygen was previously attached to the carbon skeleton and also is in the manuscript.

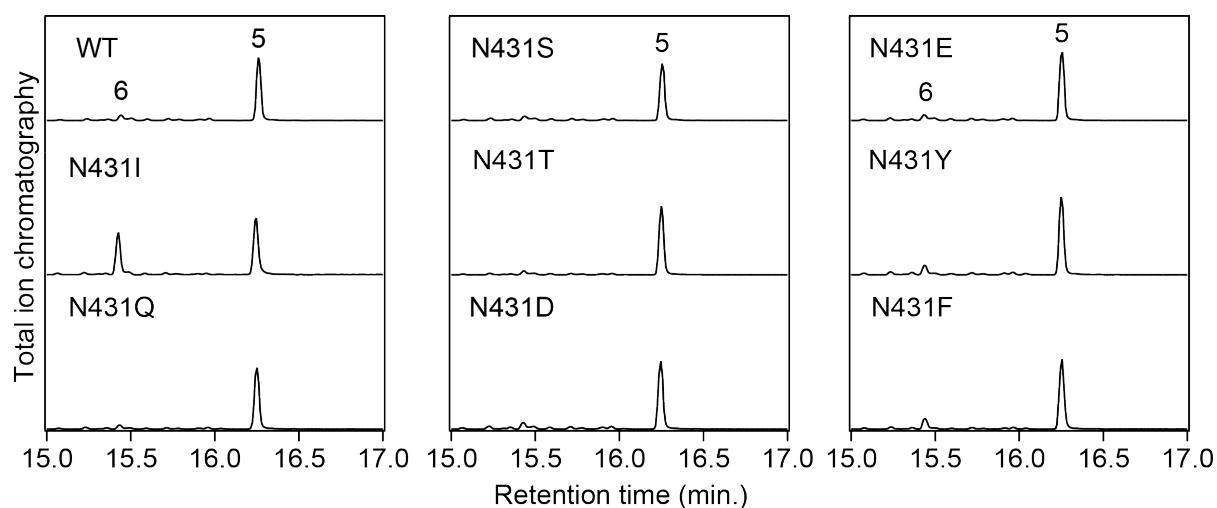


Figure S9. Mutation of N431 does not block the addition of water to **4** by SsSS. Chromatograms from GC–MS analysis.

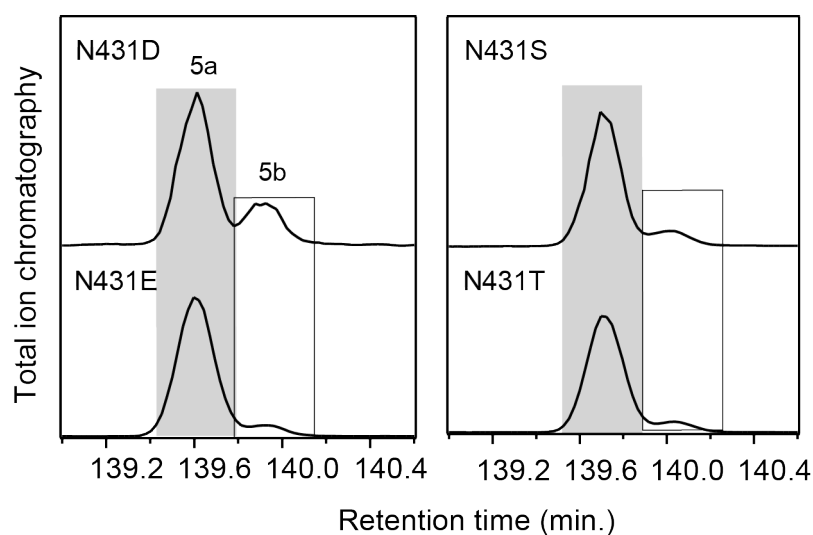


Figure S10. Substitution of polar residues for N431 does not alter SsSS product stereochemistry with **4**. Chromatograms from chiral GC–MS analysis of **5** produced by wild-type (WT) or indicated mutants of SsSS from **4** (lettering correspond to the 13-epimers as defined in the text).

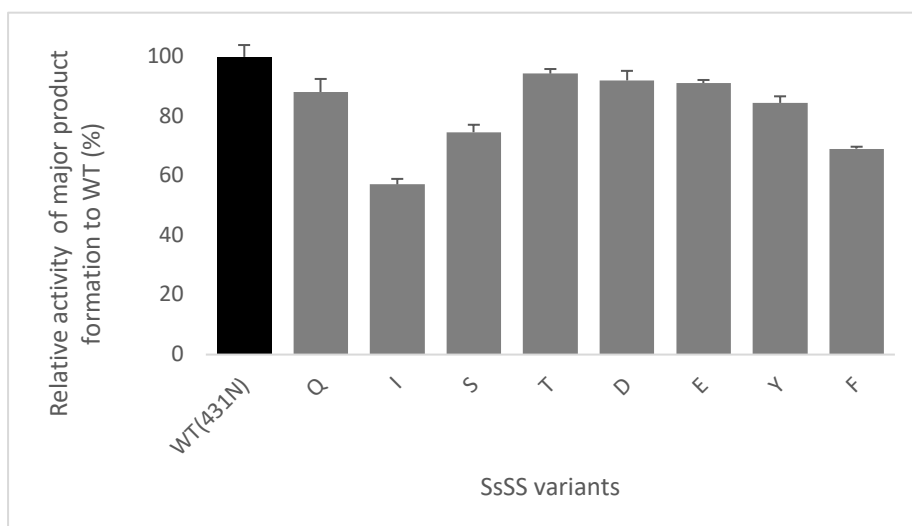


Figure S11. Biosynthetic yield of SsSS variants relative to wild-type (WT) with **4** from metabolically engineered *E. coli*. The relevant product was quantified using cembrene as an internal standard (n = 3, values represent the average of three cultures with the standard deviation shown).

Table S1: Primers for mutagenesis.

Primer name	Sequence (with mutated position underlined)
SsSS:S433C-F	TGGCTGTCGAATGGCT <u>TGCC</u> CGCTGACCGGTCTGCTG
SsSS:S433C-R	CAGCAGACCGGTCAGGCGG <u>CAG</u> CCATTCGACAGCCA
SsSS:T436C-F	AATGGCAGCCGCCTGT <u>TGCG</u> GTCTGCTGACGATGCAG
SsSS:T436C-R	CTGCATCGTCAGCAGACCG <u>CAC</u> AGGCGGCTGCCATT
SsSS:N431I-F	TCGAGCTGGCTGTCG <u>ATT</u> GGCAGCCGCCTGACCGGT
SsSS:N431I-R	ACCGGTCAGGCGGCTGCC <u>AAT</u> CGACAGCCAGCTCGA
SsSS:N431D-F	TCGAGCTGGCTGTCG <u>GAT</u> GGCAGCCGCCTGACCGGT
SsSS:N431D-R	ACCGGTCAGGCGGCTGCC <u>ATC</u> CGACAGCCAGCTCGA
SsSS:N431E-F	TCGAGCTGGCTGTCG <u>GA</u> AGGCAGCCGCCTGACCGGT
SsSS:N431E-R	ACCGGTCAGGCGGCTGCC <u>TTCC</u> GACAGCCAGCTCGA
SsSS:N431S-F	TCGAGCTGGCTGTCG <u>AGC</u> GGCAGCCGCCTGACCGGT
SsSS:N431S-R	ACCGGTCAGGCGGCTGCC <u>GCT</u> CGACAGCCAGCTCGA
SsSS:N431Q-F	TCGAGCTGGCTGTCG <u>CAG</u> GGCAGCCGCCTGACCGGT
SsSS:N431Q-R	ACCGGTCAGGCGGCTGCC <u>CTG</u> CGACAGCCAGCTCGA
SsSS:N431T-F	TCGAGCTGGCTGTCG <u>ACCG</u> GCAGCCGCCTGACCGGT
SsSS:N431T-R	ACCGGTCAGGCGGCTGCC <u>GGT</u> CGACAGCCAGCTCGA
SsSS:N431Y-F	TCGAGCTGGCTGTCG <u>TAT</u> GGCAGCCGCCTGACCGGT
SsSS:N431Y-R	ACCGGTCAGGCGGCTGCC <u>ATAC</u> GACAGCCAGCTCGA
SsSS:N431F-F	TCGAGCTGGCTGTCG <u>TTT</u> GGCAGCCGCCTGACCGGT
SsSS:N431F-R	ACCGGTCAGGCGGCTGCC <u>AAAC</u> GACAGCCAGCTCGA